Proceedings of the Thirty-fifth (2025) International Ocean and Polar Engineering Conference **www.isope.org**
Seoul/Goyang, Korea, June 1-6, 2025

ISBN 978-1-880653-74-6; ISSN 1098-6189

Influence of the Streamwise Adverse Pressure Gradient for a Fully Attached Turbulent Boundary Layer

Kangjian He[1], Jie Zhu[2], Guohua Pan[3], Decheng Wan[1]*

[1] Computational Marine Hydrodynamics Lab (CMHL), School of Naval Architecture, Ocean and Civil Engineering, Shanghai Jiao Tong University, Shanghai, China
[2] Wuhan Second Ship Design and Research Institute, Wuhan, China
[3] Ningbo Pilot Station, Ningbo Dagang Pilotage Co., Ltd., Ningbo, China

[*] Corresponding author

ABSTRACT

This paper investigates the influence of the streamwise adverse pressure gradient (APG) for an incompressible fully attached turbulent boundary layer. The turbulent flow over a 10-degree backward-facing slope is set up to generate a fully attached turbulent boundary layer with a streamwise APG. The large eddy simulation (LES) is carried out to solve the incompressible Navier-Stokes equations based on the open-source CFD toolkit OpenFOAM. Parabolized stability equations (PSE) are applied near the inlet to motivate the fully developed turbulent state. Then, detailed pressure-gradient parameters are determined, and the equilibrium state of the boundary layer is examined. A near-equilibrium state is found between = 6.7 and = 6.8, where is the boundary layer thickness at the inlet. The effect of the streamwise APG is discussed in this region by analyzing mean velocity profiles, turbulent fluctuations, and wall-pressure fluctuations along the slope.

KEY WORDS: Pressure gradient, turbulent boundary layer, large eddy simulation

INTRODUCTION

The turbulent boundary layer under a streamwise adverse pressure gradient (APG) is a critical issue in ocean and offshore engineering applications. For instance, it is commonly observed in the stern regions of underwater vehicles and marine vessels, where it significantly impacts hydrodynamic performance. Understanding the physical characteristics and fundamental mechanisms of this flow is of great importance, as the APG influences the development of the turbulent boundary layer, including turbulent fluctuations and wall pressure fluctuations. These effects directly relate to challenges in engineering design, such as optimizing hull shapes, reducing drag, and mitigating structural vibrations in marine vessels and offshore structures.

In past few years, lots of work, including experimental and numerical methods, has been conducted to investigate the influence of the streamwise APG. In particular, Krogstad and Skåre, (1995) conducted experimental investigations in a wind tunnel. They compared the turbulent structures between a zero-pressure gradient boundary layer and a boundary layer under a strong APG. They found the pressure gradient reverses the direction of the dominant turbulent diffusion, resulting in considerable turbulent transport towards the wall. (Aubertine and Eaton, 2005) investigated a turbulent boundary layer over a 4° ramp. A relatively mild APG was established. The characteristics of mean velocity and turbulent fluctuations are studied. Harun et al. (2013) conducted experimental measures in an open-return blower wind tunnel and investigated the influence of the large-scale structures of boundary layers under zero, adverse and favourable pressure gradients. Baxerres et al. (2024) used experimental methods to study the quasi-equilibrium state for a series of pressure-gradient turbulent boundary layers. These experimental studies provide abundant data and reliable research findings.

As the development of numerical methods and computational power, numerical methods are gradually applied to study the turbulent boundary subject to an APG. Lee (2017) used direct numerical simulations (DNS) to study the large-scale motions in turbulent boundary layers subjected to APGs. They found that the spatial organization of large-scale structures in the log region is significantly influenced by the strength of APGs. Yoon et al. (2018) investigated the contribution of large-scale motions to the skin friction using DNS. It was found that the large-scale energy was significantly enhanced due to the APG. Cohen and Gloerfelt (2018) used the large eddy simulation (LES) and investigated the effects of a pressure gradient beneath equilibrium turbulent boundary layers. The effects of curvature of the walls on wall pressure fluctuations were discussed. Tanarro et al. (2020) conducted LES simulations for the turbulent boundary layer over NACA0012 and NACA4412 wing sections to analyze the characteristics of the pressure gradient. Pozuelo et al. (2022) evaluated the self-similarity of the outer region using two scaling methods based on LES. Above studies provided a great reference for studying the effect of the APG. However, existing work is still limited and the physical characteristics and mechanisms are still unclear.

This paper established a turbulent boundary layer over a slope based on LES and investigates the influence of the streamwise APG.

The paper is organized as follows: First, the numerical approach is introduced. Second, details of the computational setup are discussed. Then, the characteristics of the turbulent boundary layer subject to the APG are analyzed. Finally, the conclusions are summarized.

NUMERICAL APPROACH

Governing Equations

This paper uses LES to solve the turbulent flow. In LES, large eddies are directed solved and eddies smaller than the filter size are modeled. Governing equations are unsteady filtered Navier-Stokes equations for incompressible flows:

$$\frac{\partial \tilde{u}_i}{\partial x_i} = 0 , \tag{1}$$

$$\frac{\partial \tilde{u}_i}{\partial t} + \frac{\partial \tilde{u}_i \tilde{u}_j}{\partial x_j} = -\frac{\partial \tilde{p}}{\partial x_i} + \nu \frac{\partial^2 \tilde{u}_i}{\partial x_j \partial x_j} + \frac{\partial \tau_{ij}^{\mathrm{SGS}}}{\partial x_j} , \tag{2}$$

where i = 1, 2, 3 denotes different spatial coordinates, $\tilde{p}$ and $\tilde{u}$ are filtered pressure and velocity, and ν is the molecular kinematic viscosity of the fluid. Space and time coordinates are represented by x and t. τ_{ij}^{SGS} is the subgrid-scale (SGS) stress tensor calculated by the SGS model.

AMD SGS model

In LES, eddies with large scales are directly resolved, and the effect of smaller eddies than the filtered size is represented through the SGS stress tensor $\tau_{ij}^{\mathrm{SGS}} = 2\nu_t \tilde{S}_{ij} - (1/3)\tau_{kk}^{\mathrm{SGS}} \delta_{ij}$. $\tilde{S}_{ij}$ is the resolved the resolved strain-rate tensor. ν_{SGS} is the SGS eddy viscosity calculated by the SGS model. This study uses the anisotropic minimum-dissipation (AMD) SGS model. The AMD SGS model was derived by Rozema et al. (2015) with modified Poincare inequality considering the grid anisotropy. It minimizes dissipation by ensuring the energy of sub-grid scales not increasing. In AMD SGS model, ν_{SGS} is calculated by:

$$\nu_{sgs} = C \frac{\max\left\{-\left(\delta x_k \partial_k \tilde{u}_i\right)\left(\delta x_k \partial_k \tilde{u}_j\right) S_{ij}, 0\right\}}{\left(\partial_l \tilde{u}_m\right)\left(\partial_l \tilde{u}_m\right)} \tag{3}$$

where, δx is defined as grid dimensions in different directions of the coordinate system. The AMD model is successfully applied in simulations of decaying grid turbulence (Zahiri, 2019; Zahiri and Roohi, 2021),, high-Reynolds-number rough-wall boundary-layer flow (Abkar et al., 2016), fully developed planar channel flow, and non-cavitating and cavitating flows over a 3D sphere (Zahiri, 2019). It has been proved that the AMD SGS model can provide accurate results with lower computational cost than these dynamic SGS models.

COMPUTATIONAL SETUP

Computational Domain

Fig. 1 illustrates the side view of the current computational domain. The Cartesian coordinate system *o-xyz* is used. The *x* and *y* axes are along the streamwise and normal directions, respectively, and the *z* axis is along the spanwise direction. A flat region with a length of $L_1 = 650\,\delta_0$ is set to make the flow develop into a turbulent state. δ_0 is the boundary layer thickness at the inlet. Then, a slope with a streamwise length $L_2 = 10\,\delta_0$ is set to form an APG region. The inclination angle of the slope is set as 10°, which is chosen to ensure that the boundary layer would decelerate as rapidly as possible without separating. The outlet is located $L_3 = 200\,\delta_0$ downstream from the end of the slope. The height of the computational domain at the inlet is $L_z = 300\,\delta_0$.

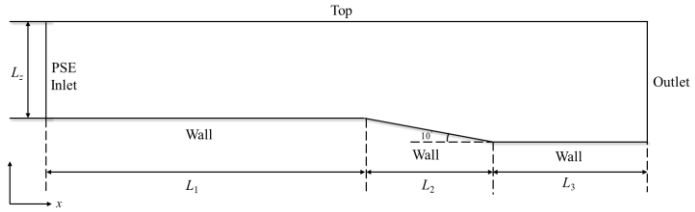

Fig. 1 The schematic of the computational domain

In past studies, many methods have been proposed to predict the transition and generate turbulent boundary layer, such as linear stability theory, parabolized stability equations (PES), and numerical trip using a suctioning and blowing boundary condition (He et al., 2024; Kumar and Mahesh, 2018; Morse and Mahesh, 2021, 2023; Wang et al., 2025). In this paper, the Parabolized Stability Equations (PSE) (Kim et al., 2019) are used to predict the laminar-to-turbulent transition by applying a boundary condition on the inlet. PSE was proposed by considering non-parallel flow effects and nonlinear interactions between instabilities during the development of laminar-to-turbulent transition. Disturbance growth in the boundary layer can be better captured in PSE than other methods. For the detailed process of PSE method please refer to (Kim et al., 2019). The freestream velocity is u_∞ = 1 m/s and the momentum thickness Reynold number is $\mathrm{Re}_\theta = \frac{u_\infty \theta}{\nu} \approx 200$ at the inlet, where θ is the boundary layer momentum thickness.

Computational Mesh

Fig. 2 shows the computational mesh around the APG region. The near-wall mesh is refined using a growth rate of 1.05 to ensure the accurate resolution of near-wall flow. The grid points are evenly spaced in both streamwise and spanwise directions. The grid resolution is set Δy_w^+ in the wall-normal direction. In the streamwise and spanwise directions, the mesh is further refined based on the work of Kim et al. (2019) to ensure the flow in the APG region well-resolved. Finally, in the transition and turbulent region, the grid resolution in streamwise and spanwise directions meets Δx^+ and Δz^+ less than 15.

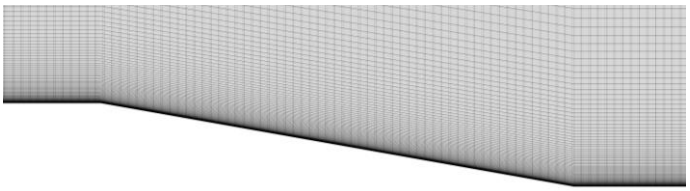

Fig. 2 Computational Mesh

Numerical Solution and Schemes

The numerical simulations are conducted using the incompressible solver *pisoFoam*, which is part of the open-source computational fluid dynamics framework, OpenFOAM. The governing equations are spatially discretized using the finite volume method (FVM). For temporal discretization, a second-order implicit backward time-stepping scheme is employed. The gradient and viscosity terms are discretized using the second-order central difference scheme, while the convective term is handled with the linear-upwind stabilized transport (LUST) scheme. To solve the coupling between velocity and pressure, the Pressure Implicit with Splitting of Operators (PISO) algorithm is utilized. For the pressure Poisson equation, the generalized geometric-algebraic multigrid (GAMG) solver is applied. The number of times a solution for pressure is set as 3 within each timestep. During the solution process, the Gauss-Seidel smoother is used in the initial stages, followed by the Diagonal incomplete-Cholesky with Gauss-Seidel (DICGaussSeidel) smoother for the final solution.

Boundary Conditions

The setting of boundary conditions is following to Kim et al. (2019). At the inlet, disturbances are introduced by superimposing a baseline laminar solution with time-varying two-dimensional velocity disturbance profiles generated using PSE. The free-stream velocity in the inlet is set as (u_∞, 0, 0). The *zeroGradient* condition in OpenFOAM is used for the pressure boundary condition. For the outlet boundary, the convective condition is used for the velocity. The fixed value p=0 is used for the pressure boundary condition. For the top boundary, the *zeroGradient* condition is used for the velocity and the fixed value p=0 is used for the pressure. No-slip boundary condition is used for the velocity and the *zeroGradient* condition is used for pressure on the solid wall. Periodic boundary condition is used in the spanwise direction to simulate the infinite domain.

Time Step and Solution Time

The time step in this study is set as $\Delta t^+ = U_0 \Delta t \cdot \delta_0^{-1} = 0.1$, satisfying that the maximum Courant number is less than 1. The simulation is conducted for over six flow-through times to discard transients and the results are sampled for another five flow-through times to collect statistics.

RESULTS AND DISCUSSIONS

Overview of the Flow Field

Fig. 3 illustrates the near-wall vortex structures during the boundary layer development, identified using the modified normalized Liutex-Omega method (Liu and Yu, 2022; Pang et al., 2023). This method utilizes the isosurface of a normalized scalar $\tilde{\Omega}_R$ to detect vortex structures, with the threshold value for the isosurface set to the recommended value of 0.52 (Zhao et al., 2020). From Fig. 3, the development of the boundary layer is clearly described. The Tollmien-Schlichting (T-S) wave is first formed and keeps the two-dimensional characteristic during the linear growth stage. Then the Λ-shape three-dimensional vortices are formed due to the enchance of the disturbances in the spanwise direction.

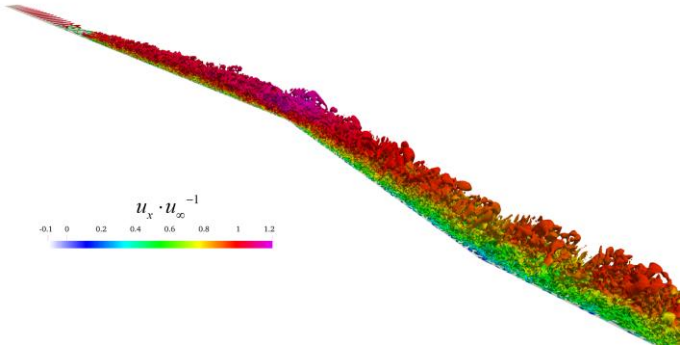

Fig. 3 Near-wall vortex structures colored by the streamwise velocity nondimensionalized by u_∞.

As the flow continues to develop downstream, the Λ shape vortices begin to be stretched and deformed and the hairpin vortex structures are formed. The interaction between different types of vortices is gradually enhanced and develops towards the turbulent state. The turbulent state is formed before the beginning of the slope, and then the vertices are influenced by the streamwise pressure gradient on the slope. The vortex structures begin to shed from the slope and form the wake vortices. However, the boundary layer is still attached on the slope and separation is not observed.

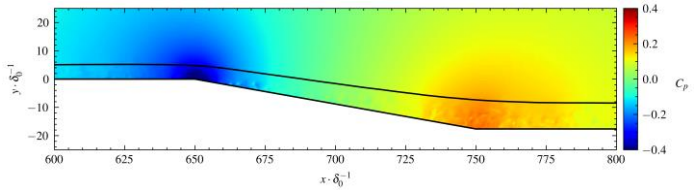

(a) Instantaneous pressure coefficient

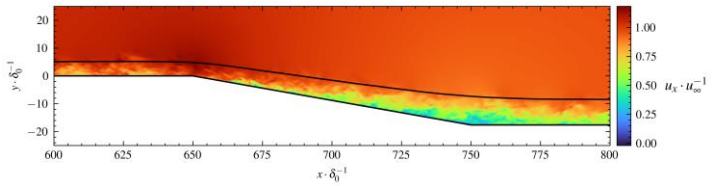

(b) Instantaneous streamwise velocity

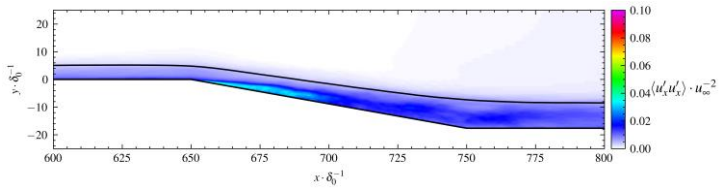

(c) Instantaneous streamwise velocity fluctuations

Fig. 4 Contours of instantaneous pressure coefficient C_p, streamwise velocity, and velocity fluctuations nondimensionalized by u_∞, in *xoy* plane.

Furthermore, Fig. 4 shows contours in the APG region of instantaneous axial velocity normalized by u_∞, pressure coefficient Cp and vorticity magnitude in *xoy* plane, plotted using Turbulucid (Mukha, 2018). The pressure coefficient is defined as

$$C_p = \frac{p - p_\infty}{0.5\rho u_\infty^2}, \tag{3}$$

where p_∞ is the reference pressure. The edge of the boundary layer is plotted using the black solid line. For the turbulent boundary layer under the APG, the conventional definition of the boundary layer thickness ($0.995\,u_\infty$) is unsuitable, as the velocity varies outside the boundary layer due to streamwise pressure gradients. As a result, alternative definitions have been proposed. Various methods for determining boundary layer thickness have been suggested, including those based on vorticity (Coleman et al., 2018; Spalart and Watmuff, 1993) and total pressure(Patel et al., 1974; Griffin et al., 2021). In this paper, the method based on $0.99\,Cp_{total,\infty}$ criterion is employed to determine the edge of the boundary layer. From Fig. 4, the adverse pressure on the slope is obviously observed. The pressure and velocity fluctuations are significant inside the boundary layer. The method based on 0.99 $Cp_{total,\infty}$ criterion effectively determines the edge of the boundary layer under the APG. The boundary thickness gradually increases under the APG.

Pressure-gradient parameters

The pressure gradient in boundary layer flows can be characterized by a variety of non-dimensional parameters according to previous studies(Aubertine and Eaton, 2005; Cohen and Gloerfelt, 2018; Parthasarathy and Saxton-Fox, 2023; Pozuelo et al., 2022; Sanmiguel Vila et al., 2017). The Clauser pressure-gradient parameter β_c, the acceleration parameter K (Kline et al., 1967), the viscous-scaled pressure gradient Δ_p are defined as

$$\beta_c = \frac{\delta^*}{\tau_w}\frac{\mathrm{d}P_e}{\mathrm{d}x}, \tag{4}$$

$$K = \frac{\nu}{U_e^2}\frac{\mathrm{d}U_e}{\mathrm{d}x}, \tag{5}$$

$$\Delta_p = \frac{\nu}{\rho u_\tau^3}\frac{\mathrm{d}P_e}{\mathrm{d}x}, \tag{6}$$

$$\Lambda = \frac{\delta}{\rho U_e^2(\mathrm{d}\delta/\mathrm{d}x)}\frac{\mathrm{d}P_e}{\mathrm{d}x}, \tag{7}$$

where U_e and P_e are the mean streamwise velocity and local static pressure at the edge of the boundary layer. δ are δ^* are the boundary layer thickness and displacement thickness. ρ and ν are the density and kinematic viscosity of the fluid. τ_w is the wall stress and u_τ is the friction velocity. The turbulent boundary layer is also characterized by its shape factor H and the defect shape factor G defined as

$$H = \frac{\delta^*}{\theta}, \tag{8}$$

$$S = \frac{U_e}{u_\tau}, \tag{9}$$

$$G = S\left(1 - \frac{1}{H}\right), \tag{10}$$

The equilibrium for the boundary layers subjected to a pressure gradient is an important characteristic. A turbulent boundary layer at the equilibrium state is significant for wavenumber-frequency analysis and avoiding the effect of the dependence on the upstream history and the way the gradient is applied (Cohen and Gloerfelt, 2018). Next, we discuss the equilibrium characteristic of the present turbulent boundary layer. Here, we use the criterion that the turbulent boundary layer under the APG achieves an equilibrium region if the above non-dimensional parameters maintain constant.

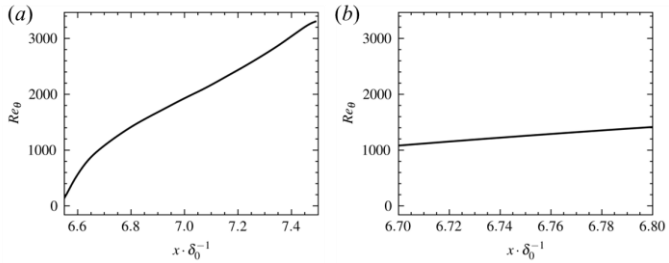

Fig. 5 Streamwise evolution of (a) Re_θ on the slope and (b) the enlarged region between $x \cdot \delta_0^{-1}$ = 6.7 and $x \cdot \delta_0^{-1}$ = 6.8.

Fig. 5 present the streamwise evolution of the momentum thickness Reynold number Re_θ on the slope. As the development of the boundary layer on the slope, the boundary layer momentum thickness increases and hence Re_θ increases. We enlarge the region between $x \cdot \delta_0^{-1}$ = 6.7 and $x \cdot \delta_0^{-1}$ = 6.8 and found Re_θ increases linearly with $x \cdot \delta_0^{-1}$. The pressure gradient in this region will be analyzed and a equilibrium state will be found in this region.

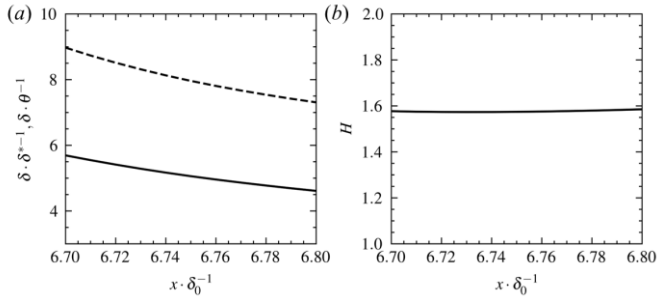

Fig. 6 Streamwise evolution of ratios of boundary-layer thicknesses: (a) $\delta \cdot \delta^{*-1}$, $\delta \cdot \theta^{-1}$, and (b) shape factor $H = \delta^* \cdot \theta^{-1}$ between $x \cdot \delta_0^{-1}$ = 6.7 and $x \cdot \delta_0^{-1}$ = 6.8.

Fig. 6 shows the streamwise evolution of ratios of boundary-layer thicknesses: (a) $\delta \cdot \delta^{*-1}$, $\delta \cdot \theta^{-1}$, and shape factor $H = \delta^* \cdot \theta^{-1}$. Fig. 7 presents the streamwise evolution of corresponding pressure gradient parameters. One can see that $\delta \cdot \delta^{*-1}$ and $\delta \cdot \theta^{-1}$ decrease linearly as the development of the turbulent boundary layer. Pressure gradient including the shape factor $H = \delta^* \cdot \theta^{-1}$, the Clauser pressure-gradient parameter β_c, the acceleration parameter K, the viscous-scaled pressure gradient Δ_p, and defect shape factor G are nearly constant between $x \cdot \delta_0^{-1}$ = 6.7 and $x \cdot \delta_0^{-1}$ = 6.8. Corresponding values are H = 1.58, β_c = 2.00, K =-1.70, Δ_p = 0.26, and G = 8.70. Therefore, a

near-equilibrium is achieved between $x \cdot \delta_0^{-1}$ = 6.7 and $x \cdot \delta_0^{-1}$ = 6.8. The value of β_c is relatively small, indicating the present pressure gradient is moderate.

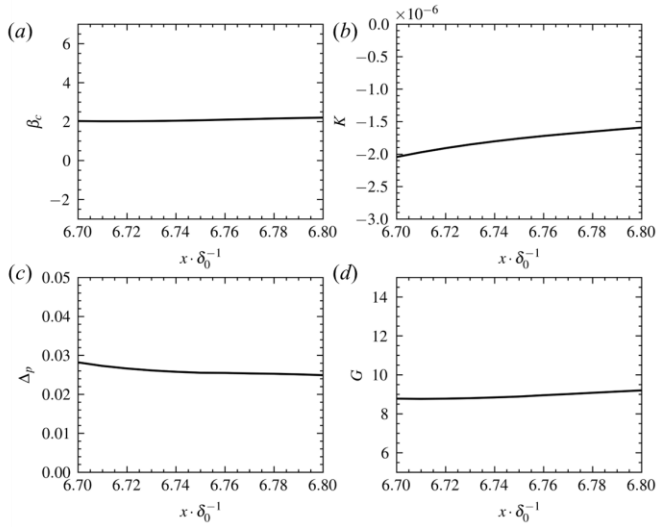

Fig. 7 Streamwise evolution of (a) the Clauser pressure-gradient parameter β_c, (b) the acceleration parameter K, (c) the viscous-scaled pressure gradient Δ_p, and (d) defect shape factor G between $x \cdot \delta_0^{-1}$ = 6.7 and $x \cdot \delta_0^{-1}$ = 6.8.

Time-averaged statistics

Fig. 8 illustrates eleven profiles between $x \cdot \delta_0^{-1}$ = 6.7 and $x \cdot \delta_0^{-1}$ = 6.8 of the mean streamwise velocity. The interval in the flow direction for every profile is 0.01 δ_0 and the color is marked from white to black. The distribution is non-dimensionalized using the wall units. The wall units are defined by the kinematic viscosity ν and friction velocity u_τ. As we can see, all the profiles collapse well, especially in the viscous sub-layer and buffer layer region. This is expected due to the mild magnitude of the pressure gradient.

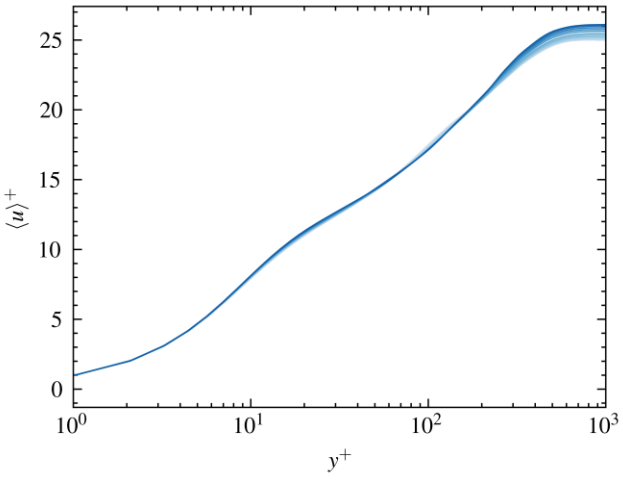

Fig. 8 Mean streamwise velocity profiles in wall units: eleven profiles between $x \cdot \delta_0^{-1}$ = 6.7 and $x \cdot \delta_0^{-1}$ = 6.8.

Turbulent fluctuations

Furthermore, Fig. 9 illustrates eleven profiles of the streamwise velocity fluctuations between $x \cdot \delta_0^{-1}$ = 6.7 and $x \cdot \delta_0^{-1}$ = 6.8. From Fig. 9, it is seen that a degree of self-similarity within the very near-wall region (y^+ < 10). Near-wall peaks in the streamwise velocity fluctuations are observed in the profiles and located at $y^+ \approx 12$. The peak value mildly increase as $x \cdot \delta^{-1}$ increases while corresponding location remain unchanged in wall units. Otherwise, outer peaks are observed in profiles of the streamwise velocity fluctuations. The outer peaks move outward with increasing strength and width as $x \cdot \delta^{-1}$ increases. The appearance of outer peaks in streamwise velocity fluctuation profiles is a typical feature of turbulent boundary layers under APGs (APG), leading to the amplification of large-scale turbulent structures.

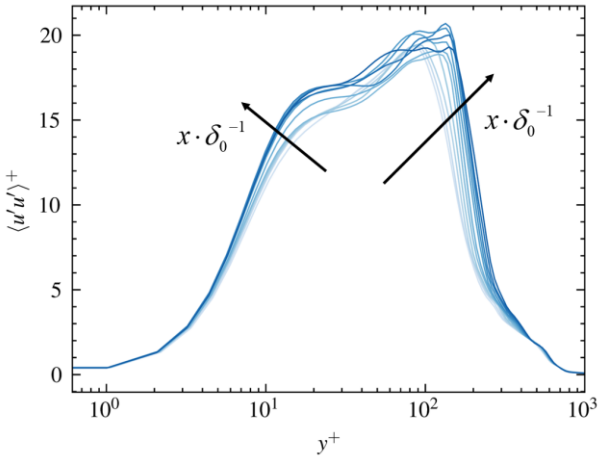

Fig. 9 Profiles of the streamwise velocity fluctuations in wall units: eleven profiles between $x \cdot \delta_0^{-1}$ = 6.7 and $x \cdot \delta_0^{-1}$ = 6.8.

Wall pressure fluctuations

To study the characteristics of the wall pressure fluctuations, we calculate the frequency power spectra using the fast Fourier transform algorithm in Python by segmenting the time series into 30 blocks of 2000 samples in each block, along with a 50% overlap and Hanning window. Fig. 10 shows the frequency power spectra for various streamwise positions.

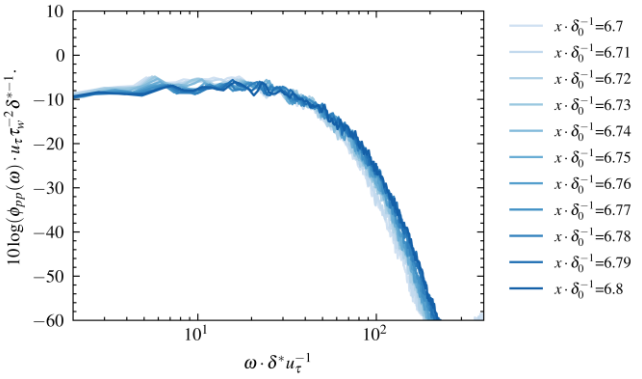

Fig. 10 Frequency power spectra with mixed scalings for different positions between $x \cdot \delta_0^{-1}$ = 6.7 and $x \cdot \delta_0^{-1}$ = 6.8.

The famous mixed scaling is used to non-dimensionalize the spectra, which τ_w is the pressure scale, and $\delta^* u_\tau^{-1}$ is the frequency scale. The resulting non-dimensional spectrum from all locations collapses well. The magnitude of the non-dimensional spectrum initially exhibits a mild increase at low frequencies and then decreases as the frequency ω increases.

CONCLUSIONS

In this paper, a turbulent boundary layer under a moderate APG is established by a 10° slope. The turbulent boundary layer is fully developed and attached to the wall, which means the separation is not observed. The near-equilibrium region is found by analyzing the pressure-gradient parameters. In this region, the streamwise velocity profiles collapse well, especially in the viscous sub-layer and buffer layer region. The streamwise turbulent fluctuations collapse well in the sub-layer region and the peak values of mean streamwise velocity fluctuations mildly increases as $x \cdot \delta^{-1}$ increases. For the wall pressure fluctuations, the resulting non-dimensional spectrum from all locations collapses well. The magnitude of the non-dimensional spectrum initially exhibits a mild increase at low frequencies and then decreases as the frequency ω increases.

ACKNOWLEDGEMENTS

This work is supported by the National Natural Science Foundation of China (52131102), to which the authors are most grateful.

REFERENCES

Abkar, M, Bae, HJ, and Moin, P (2016). "Minimum-dissipation scalar transport model for large-eddy simulation of turbulent flows," *Phys Rev Fluids*, 1(4), 041701.

Aubertine, CD, and Eaton, JK (2005). "Turbulence development in a non-equilibrium turbulent boundary layer with mild adverse pressure gradient," *J Fluid Mech*, 532, 345–364.

Baxerres, V, Vinuesa, R, and Nagib, H (2024). "Evidence of quasiequilibrium in pressure-gradient turbulent boundary layers," *J Fluid Mech*, 987, R8.

Cohen, E, and Gloerfelt, X (2018). "Influence of pressure gradients on wall pressure beneath a turbulent boundary layer," *J Fluid Mech*, 838, 715–758.

Coleman, GN, Rumsey, CL, and Spalart, PR (2018). "Numerical study of turbulent separation bubbles with varying pressure gradient and Reynolds number," *J Fluid Mech*, 847, 28–70.

Griffin, KP, Fu, L, and Moin, P (2021). "General method for determining the boundary layer thickness in nonequilibrium flows," *Phys Rev Fluids*, 6(2), 024608.

Harun, Z, Monty, JP, Mathis, R, and Marusic, I (2013). "Pressure gradient effects on the large-scale structure of turbulent boundary layers," *J Fluid Mech*, 715, 477–498.

He, K, Zhou, F, Zhao, W, and Wan, D (2024). "Wall-Modeled Large Eddy Simulation for a Highly Decelerated Axisymmetric Turbulent Boundary Layer," *Proceedings of the Thirty-Fourth (2024) International Ocean and Polar Engineering Conference*, Rhodes, Greece, 1916–1922.

Kim, M, Lim, J, Kim, S, Jee, S, Park, J, and Park, D (2019). "Large-eddy simulation with parabolized stability equations for turbulent transition using OpenFOAM," *Computers & Fluids*, 189, 108–117.

Kline, SJ, Reynolds, WC, Schraub, FA, and Runstadler, PW (1967). "The structure of turbulent boundary layers," *J Fluid Mech*, 30(4), 741–773.

Krogstad, P-Å, and Skåre, PE (1995). "Influence of a strong adverse pressure gradient on the turbulent structure in a boundary layer," *Physics of Fluids*, 7(8), 2014–2024.

Kumar, P, and Mahesh, K (2018). "Large-eddy simulation of flow over an axisymmetric body of revolution," *Journal of Fluid Mechanics*, 853, 537–563.

Lee, JH (2017). "Large-scale motions in turbulent boundary layers subjected to adverse pressure gradients," *J Fluid Mech*, 810, 323–361.

Liu, C, and Yu, Y (2022). "Mathematical foundation of Liutex theory," *J Hydrodyn*, 34(6), 981–993.

Morse, N, and Mahesh, K (2021). "Large-eddy simulation and streamline coordinate analysis of flow over an axisymmetric hull," *J Fluid Mech*, 926, A18.

Morse, N, and Mahesh, K (2023). "Tripping effects on model-scale studies of flow over the DARPA SUBOFF," *J Fluid Mech*, 975, A3.

Mukha, T (2018). "Turbulucid: A Python Package for Post-Processing of Fluid Flow Simulations," *JORS*, 6(1), 23.

Pang, B, Yu, Z, Yan, B-W, Wang, Y, and Liu, C (2023). "Identification of vortex boundaries in two-dimensional incompressible flows based on the Liutex-shear interaction," *J Hydrodyn*, 35(5), 825–831.

Parthasarathy, A, and Saxton-Fox, T (2023). "A family of adverse pressure gradient turbulent boundary layers with upstream favourable pressure gradients," *J Fluid Mech*, 966, A11.

Patel, VC, Nakayama, A, and Damian, R (1974). "Measurements in the thick axisymmetric turbulent boundary layer near the tail of a body of revolution," *Journal of Fluid Mechanics*, 63(2), 345–367.

Pozuelo, R, Li, Q, Schlatter, P, and Vinuesa, R (2022). "An adverse-pressure-gradient turbulent boundary layer with nearly constant $\beta \approx 1.4$ up to $Re\theta \approx 8700$," *J Fluid Mech*, 939, A34.

Rozema, W, Bae, HJ, Moin, P, and Verstappen, R (2015). "Minimum-dissipation models for large-eddy simulation," *Physics of Fluids*, 27(8), 085107.

Sanmiguel Vila, C, Örlü, R, Vinuesa, R, Schlatter, P, Ianiro, A, and Discetti, S (2017). "Adverse-Pressure-Gradient Effects on Turbulent Boundary Layers: Statistics and Flow-Field Organization," *Flow Turbulence Combust*, 99(3–4), 589–612.

Spalart, PR, and Watmuff, JH (1993). "Experimental and numerical study of a turbulent boundary layer with pressure gradients," *J Fluid Mech*, 249(1), 337.

Wang, G, Liu, Y, Wang, S, and He, G (2025). "Assessment of the Reynolds-stress model-based hybrid RANS/LES method for junction flow around a fully appended underwater vehicle," *Ocean Engineering*, 318, 120073.

Yoon, M, Hwang, J, and Sung, HJ (2018). "Contribution of large-scale motions to the skin friction in a moderate adverse pressure gradient turbulent boundary layer," *J Fluid Mech*, 848, 288–311.

Zahiri, A-P (2019). "Anisotropic minimum-dissipation (AMD) subgrid-scale model implemented in OpenFOAM: Verification and assessment in single-phase and multi-phase flows.,"

Zahiri, A-P, and Roohi, E (2021). "Assessment of anisotropic minimum-dissipation (AMD) subgrid-scale model: Gently-curved backward-facing step flow," *Int J Mod Phys C*, 32(05), 2150068.

Zhao, W, Wang, J, and Wan, D (2020). "Vortex identification methods in marine hydrodynamics," *J Hydrodyn*, 32(2), 286–295.